



DEFENSE TECHNICAL INFORMATION CENTER

Information for the Defense Community

DTIC[®] has determined on 11 / 08 / 13 that this Technical Document has the Distribution Statement checked below. The current distribution for this document can be found in the DTIC[®] Technical Report Database.

DISTRIBUTION STATEMENT A. Approved for public release; distribution is unlimited.

© COPYRIGHTED. U.S. Government or Federal Rights License. All other rights and uses except those permitted by copyright law are reserved by the copyright owner.

DISTRIBUTION STATEMENT B. Distribution authorized to U.S. Government agencies only (fill in reason) (date of determination). Other requests for this document shall be referred to (insert controlling DoD office).

DISTRIBUTION STATEMENT C. Distribution authorized to U.S. Government Agencies and their contractors (fill in reason) (date determination). Other requests for this document shall be referred to (insert controlling DoD office).

DISTRIBUTION STATEMENT D. Distribution authorized to the Department of Defense and U.S. DoD contractors only (fill in reason) (date of determination). Other requests shall be referred to (insert controlling DoD office).

DISTRIBUTION STATEMENT E. Distribution authorized to DoD Components only (fill in reason) (date of determination). Other requests shall be referred to (insert controlling DoD office).

DISTRIBUTION STATEMENT F. Further dissemination only as directed by (insert controlling DoD office) (date of determination) or higher DoD authority.

Distribution Statement F is also used when a document does not contain a distribution statement and no distribution statement can be determined.

DISTRIBUTION STATEMENT X. Distribution authorized to U.S. Government Agencies and private individuals or enterprises eligible to obtain export-controlled technical data in accordance with DoDD 5230.25; (date of determination). DoD Controlling Office is (insert controlling DoD office).

Final Report

Date 03-12-2013

Project Title: Laser beam induced current (LBIC) study of IR detector materials

DARPA contract #: W911NF-11-2-0070

Project Director: Dr. Nibir Dhar (DARPA/MTO)

Technical Monitor: Dr. Yuanping Chen (ARL)

PI: Prof. Yong Zhang (UNC-Charlotte)

Period: 9/6/2011 – 9/5/2012 (initial), 6-month no cost extension to 3/5/2013

Summary of activities and results:

- 1. Demonstration of IR-LBIC spatial mapping of a MCT-FPA device using a 1450nm laser from both back and front sides**
- 2. Unusual LBIC spatial mapping results of a MCT-FPA device from the front (electrode) side using a 532nm laser**
- 3. Demonstration of LBIC spatial mapping of an InAs/GaSb IR detector using a 532 nm laser at 10 K**
- 4. PL spatial mapping of an isolated dislocation in GaAs, leading to general understanding of the interplay between point and extended defects on carrier diffusion in semiconductors**
- 5. PL spatial mapping of CdTe epilayers with different growth conditions**
- 6. PL spatial mapping of ZnTe epilayers with different growth conditions, from front surface and cleaved edge**
- 7. MCT epilayer transmission and reflection measurements**

20130924403

1. Demonstration of IR-LBIC spatial mapping of MCT-FPA device using a 1450nm laser

We upgrade a confocal micro-Raman system (Horiba LabRam HR800) so that multiple correlated spatial mappings, including Raman, PL, EL, LBIC, and reflectance, can all be performed on the exactly same sample area with sub-micron spatial resolution, and furthermore SEM/EDS can be measured from the same area afterward. With adding two IR lasers (808 nm and 1450 nm), we can perform the LBIC measurement in the spectra range that is more relevant to the IR materials. We have set-up a versatile optical characterization system for a wide variety semiconductor materials and applications (e.g., photo-detector, PV device, LED, laser) from UV to NIR.

We have performed preliminary LBIC measurements on a MCT-FPA device provided by Dr. Priyalal Wijewarnasuriya (ARL) using a 1450 nm laser at 300 K. The wavelength used is below the bandgap of the Si substrate, therefore, the measurement can be performed from the backside of the device, as in the real application. We also tested it on the front side, although this side is mostly covered by the metallic electrodes, the results are very interesting on its own. In the LBIC mapping measurement, the photocurrent is measured point-by-point when a focused laser beam is scanned over a pre-defined area. An area of $20\mu\text{m}\times 20\mu\text{m}$ was used in our measurements. Figure 1 shows the LBIC mapping data together with an optical image of the mapped area from the back side or the IR transparent side; Figure 2 from the front side or the IR non-transparent side for the same area (within a few μm accuracy).

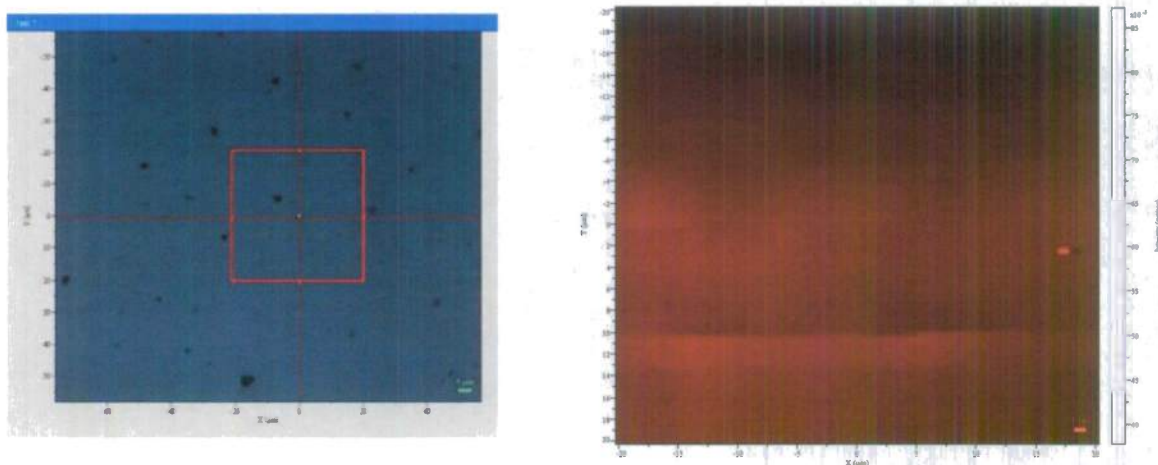


Fig.1 A LBIC map of a MCT-FPA measured from the transparent (back) side using a 1450 nm laser. Left – an optical image with the mapped area, $20\mu\text{m}\times 20\mu\text{m}$ indicated by the red box; Right – LBIC mapping data (Laser power ≈ 2 mW, maximum current ~ 17 nA, under zero bias.

It puzzled us that the mapping yielded no clearly observable features that could be associated with defects. Only until recently, we have come to realize that the IR laser was not appropriately focused on the sample, because we were inexperienced in using this IR laser that is invisible in the imaging camera. In the future, we should acquire an IR camera for better monitoring the laser focusing and beam alignment. The front side with metallic electrode is expected to be opaque to both IR and visible light. However, decent size photocurrents were observed using both IR and visible lasers. As shown in Fig.2, for the 1450 nm laser, the maximum signal from the front side is reduced by approximately a factor of 600. Given the fact that the electrode thickness is in the order of $0.5\mu\text{m}$, this reduction is much smaller than one would expect. This could be an important serendipity worth further investigation. The effect is more prominent and interesting when the 532nm laser was used with higher spatial resolution (to be reported in the next section).

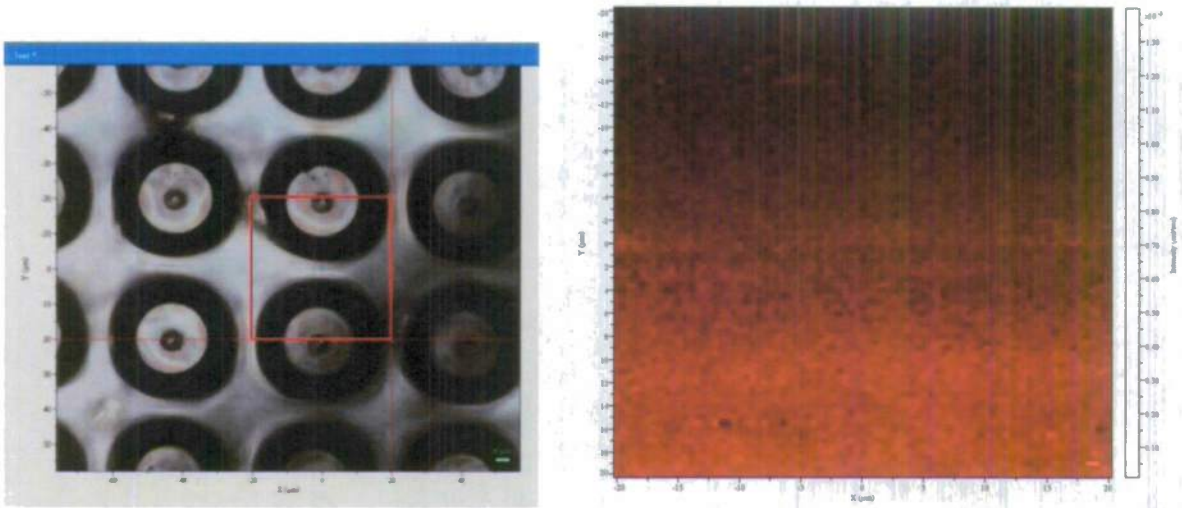


Fig.2 A LBIC map of a MCT-FPA measured from the non-transparent (front) side using a 1450 nm laser. Left – an optical image with the mapped area, $20\mu\text{m} \times 20\mu\text{m}$ indicated by the red box; Right – LBIC mapping data (Laser power ≈ 2 mW, maximum current ~ 27 pA, under zero bias).

2. Unusual LBIC spatial mapping results a MCT-FPA device from the front (electrode) side using a 532nm laser

The LBIC mapping was performed on the same area as shown in Fig.2. Evidently, the LBIC mapping reflects the features on the surface of the sample. The bright region has somewhat higher external quantum efficiency (EQE) than that with 1450 nm. The exact EQE value remains to be calibrated. However, it is estimated to be about a factor of 100 smaller than that at 1450 nm measured from the transparent side. On a different component, the signal with 532 nm was found to

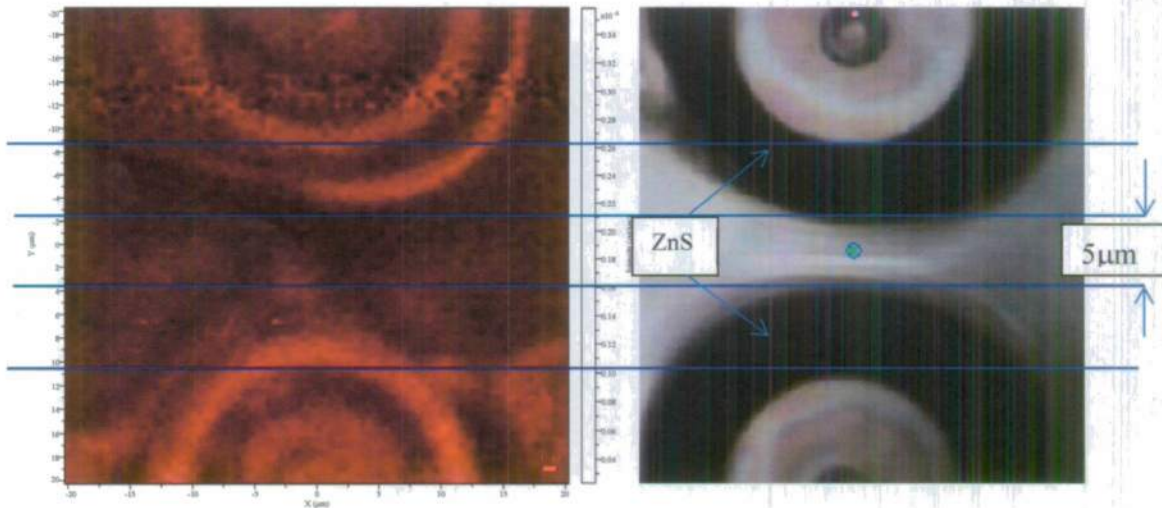


Fig.3 A LBIC map of a MCT-FPA measured from the non-transparent (front) side using a 532 nm laser. Right – an optical image of the mapped area, $20\mu\text{m} \times 20\mu\text{m}$; Left – LBIC mapping data (Laser power ≈ 0.3 mW, maximum current ~ 7 pA, under zero bias).

be ~10 times stronger than the one of Fig.3, which makes this finding very intriguing.

3. Demonstration of LBIC spatial mapping of an InAs/GaSb IR detector using a 532 nm laser at 10 K

We have tested the LBIC capability on an InAs/GaSb type II superlattice IR detector (~ 9 μm) provided by Prof. Shun-Lien Chuang's group (UIUC). Because of no measurable signal at room temperature, the device was cooled down to 10 K, which also made us testing the low temperature operation of the system. Figure 4 shows the LBIC mapping results of a $20\mu\text{m}\times 20\mu\text{m}$ at three laser intensities. Two interesting observations are with increasing power, (1) the percentage of bright area over the total area increases, and (2) the spatial variation reduces, which seem to suggest that the lower efficiency regions are passivated by the increased carrier density, presumably by saturating the nonradiative centers. The results indicate that if the whole device behaves the same as the few bright spots at the low illumination density, the overall performance of the device could improve substantially.

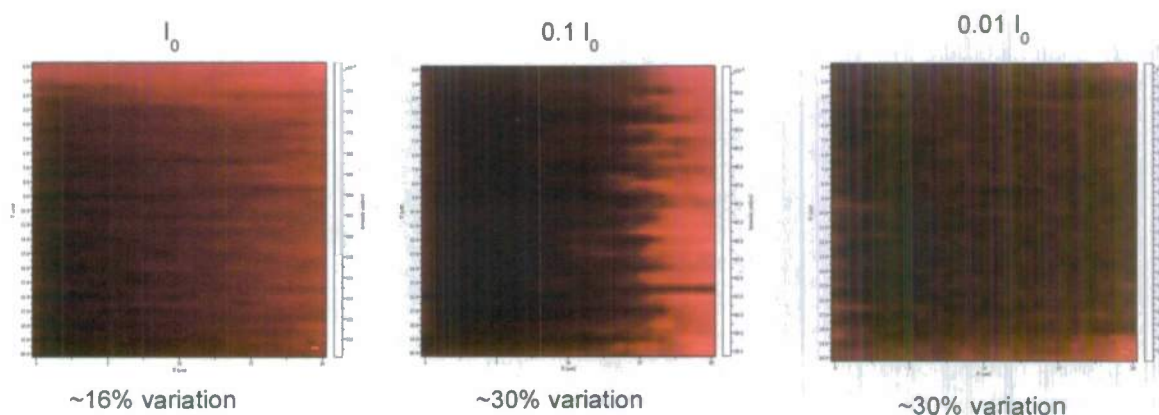


Fig.4 LBIC maps of an InAs/GaSb IR detector measured at 10 K using a 532nm laser at three powers under zero bias. The mapping area is $20\mu\text{m}\times 20\mu\text{m}$. The variation indicates the contrast between the highest and lowest regions.

4. PL spatial mapping of an isolated dislocation in GaAs, leading to general understanding of the interplay between point and extended defects on carrier diffusion in semiconductors

Although GaAs is not a material of direct interest to this project, it was used to derive fundamental understanding of the impact of an isolated extended defect, such as a threading dislocation, on the carrier diffusion and recombination, because we was able to obtain a GaInP/GaAs/GaInP double heterostructure with $< 10^3/\text{cm}^2$ dislocation density in the GaAs layer. The material was provided by Dr. Mark Wanlass of NREL. Sometimes it is rather puzzling that a device with a relative high dislocation density can perform reasonably well or reducing the defect dislocation does not seem to significantly improve the device performance. We performed spatially resolved PL mapping near one isolated extended defect in the GaAs epilayer with varying excitation density, with the results shown in Figure 5. As expected, the defect results in a dark region centered at the defect, because the defect acts like a sink that captures all the carriers that diffuse to the defect

site. It is most interesting to see that the size of the dark region varies with the excitation density in a non-monotonic manner: it firstly increases with reducing laser power, indicating an increase in the diffusion length; however, it decreases when the laser decreases further, suggesting a decrease in the diffusion length. The explanation is as follows: at very low excitation density and thus carrier density, the invisible point defects impede the carrier diffusion, which is perhaps the situation most relevant to the IR detector operation; with increasing the excitation density, the saturation of the point defects results in the longer diffusion length, and the dislocation becomes more detrimental; with further increasing the excitation density, the carrier life time decreases, leading to the decrease in the diffusion length. The finding suggests that at low carrier density, the effect of the extended defects is less significant. One more important finding is that after illuminating the defect at a high power that yields a high carrier density for merely a few second, which is perhaps relevant to a semiconductor laser operated under a high injection current, a permanent modification occurs to the defect, namely the polarity of the defect seems to have switched from a hole trap to an electron trap, resulting in a much larger effective range of the defect (by \sim a factor of 10). This finding is highly relevant to the semiconductor laser or power electronic device and suggests ways to minimize the impact of the defect through the device design. The results have been reported in a recent Appl. Phys. Lett. paper. (Gfroerer, Zhang, Wanlass, Appl. Phys. Lett., 102, 0122114, 2013).

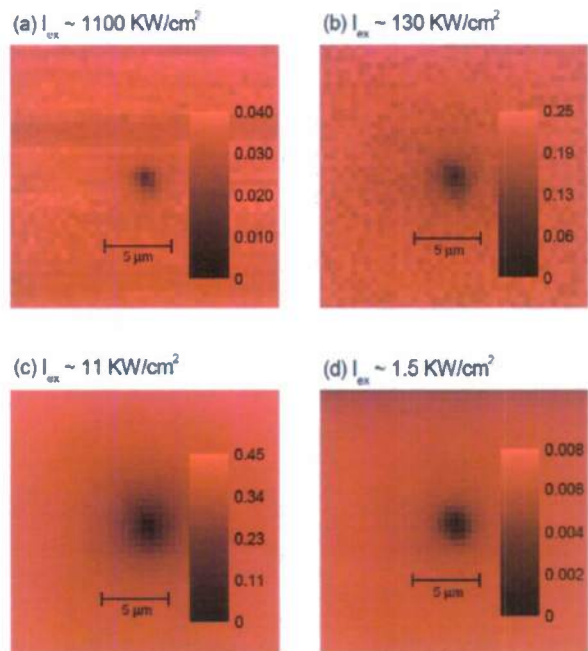


Fig.5 Plan-view confocal PL maps of an isolated dislocation in GaAs over a wide range of photoexcitation intensities I_{ex} . (I_{ex} values do not include reflection loss.) Greyscale values are estimates of radiative efficiency—the ratio of photons emitted to photons absorbed.

We have developed a theoretical model that can extract the diffusion length from the data like those shown in Fig.5. We have found that the widely used formula $\exp(-r/L)$, with L being the diffusion length, for fitting the intensity variation on the plan is in fact incorrect for the measurement mode of local excitation and local detection as adopted in the PL mapping. The spatial dependence is instead close to $\exp(-2r/L)$, which implies that the spatial resolution could be substantially better than the widely believed one corresponding to the diffusion length.

5. PL spatial mapping of CdTe epilayers with different growth conditions

We have performed spatially resolved PL measurements on a set of CdTe epilayers grown on Si-(211) substrates. Table 1 summarizes the materials parameters and the results of our μ -PL

Table 1 CdTe epilayers grown on Si-(211) substrates.

Sample	Thick (mm)	Growth Temperatu re (°C)	FWH M (arcse c)	# of Anneali ng Cycles	EPD (10^7c m^{-2})	Average PL Intensity (normalize d)
32207	8.95	280.0	110	0	2.7	0.527
32707	8.8	280.0	86	2	1.6	0.964
40307	9	280.0	79	4	0.98	0.753
32807	8.8	280.0	56	6	0.13	0.799
32607	8.9	280.0	61	8	0.077	1.000
32307	8.8	280.0	58	10	0.043	0.911

measurements. The characterizations done at ARL have revealed a general correlation between the number of annealing cycles with XRD FWHM and EPD, whereas our data further show a general trend that the density of the PL dark spots reduces with increasing the annealing cycle. Figure 6 shows the comparison between the PL maps of the 6 samples over a $20\mu\text{m}\times 20\mu\text{m}$ area, whereas Figure 7 depicts the histogram plots of the data (note that both the horizontal (intensity) and vertical (count) ranges are kept the same for all the samples). It appears that the sample with annealing cycle # = 8 shows the lowest number of the dark spots, highest intensity, and most uniform. A new set of etched samples has been provided by Dr. Y.-P. Chen for further investigating the defects. They are yet to be measured.

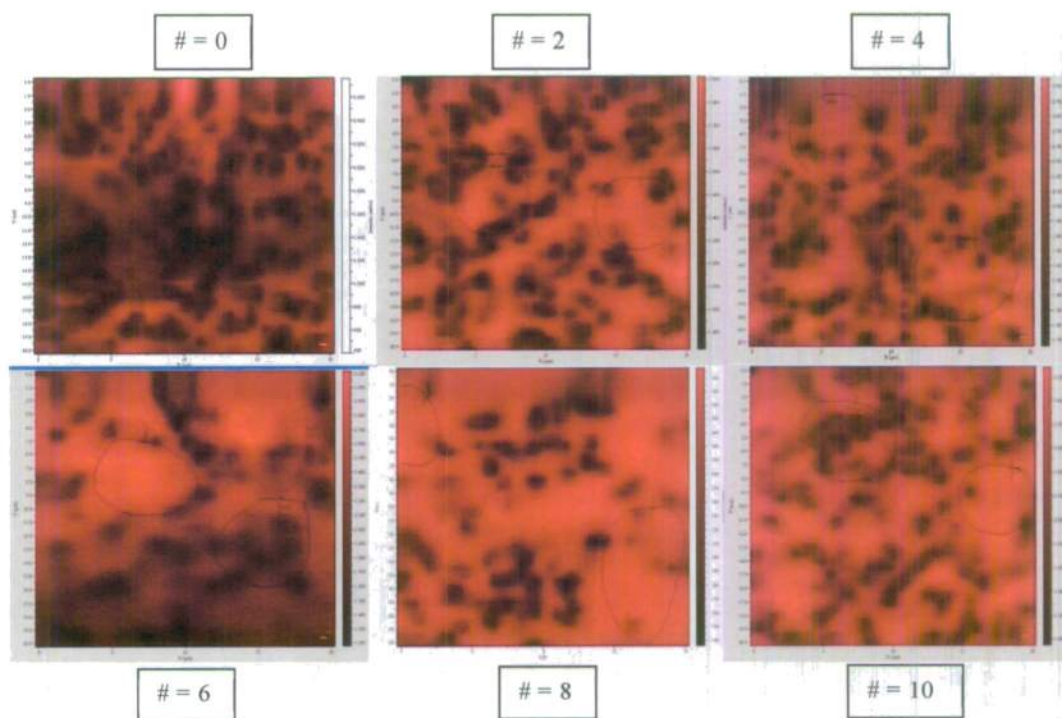


Fig.6 PL maps of CdTe epilayers with different annealing cycles.

Besides offering a qualitative picture of the impact of the defects, manifested as the dark spots in the PL map, each mapping result can in principle provide more quantitative information of the material, such as the diffusion length of the material in a hypothetical situation where all the defects were removed while keeping the microscopic structure of the material unchanged. We are currently developing a modeling method to extract such a diffusion length from the data like any of the panels shown in Fig.6, as long as the defect density is not too high, for instance the data for sample with # = 8 or # = 10. For a low defect density region, we could treat the data as though there were only one defect, for instance the circled area at the middle right region of # = 10, and get an estimate of the “intrinsic” diffusion length to be $\sim 1.4 \mu\text{m}$ using the modeling method mentioned above.

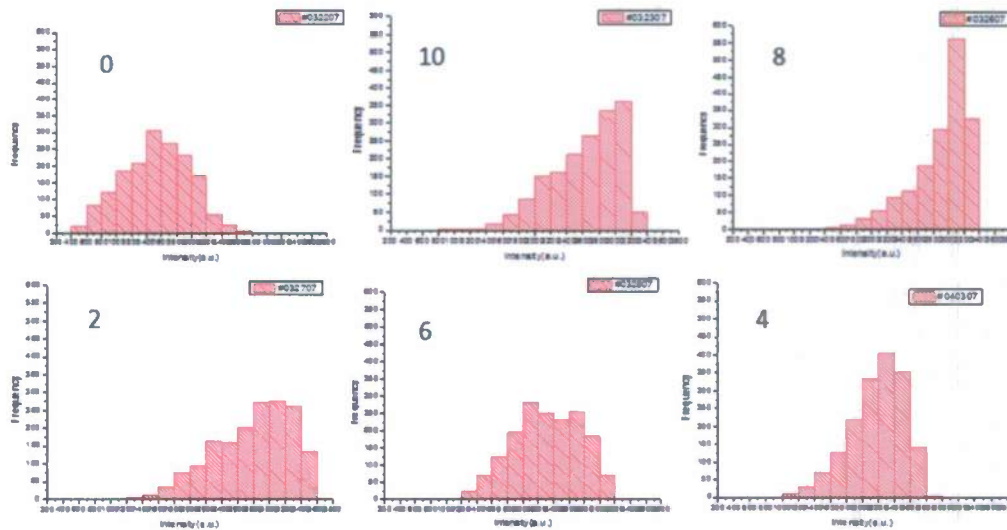


Fig.7 Histogram plots for the PL mapping data shown in Fig.6.

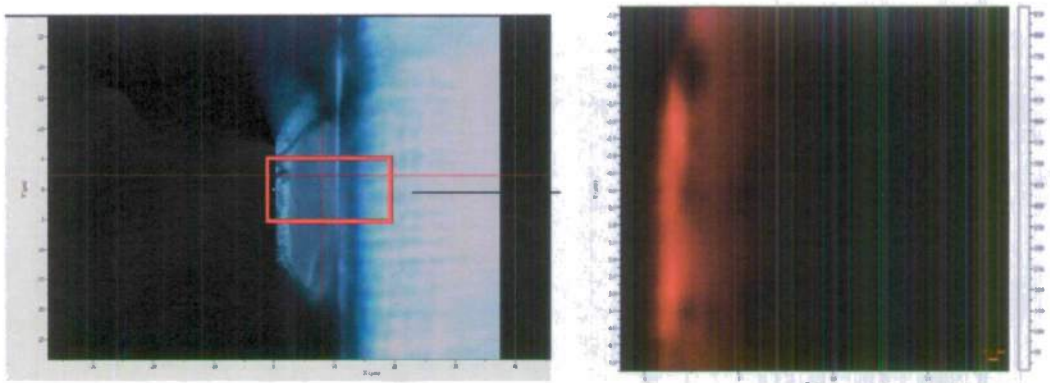


Fig.8 Cleaved edge PL mapping of sample # = 10. Left – optical image, Right – PL image.

We also attempted to do the PL mapping from the cleaved edge to examine the effect of the growth interruptions (the annealing cycles). Figure 8 shows the PL mapping result for the sample # = 10. One could see some stratification on the PL image along the growth direction, and as expected, the PL intensity is stronger for the material close to the top of the epilayer. The sample

was not cleaved well in this testing, because of the substrate orientation being (211). We would like to try a different edge in the future.

6. PL spatial mapping of ZnTe epilayers with different growth conditions, from front surface and cleaved edge

A. Front Surface Photoluminescence Spectra

A set of ZnTe samples with varying nuclear and growth temperature were provided by Dr. Yuan-Ping Chen (ARL). These ZnTe epitaxy samples were grown on Si 211 substrate. Because of the relatively large lattice mismatch, they typically exhibit substantial amount of defects in the ZnTe epilayers. Plan-view photoluminescence spectra of the ZnTe epilayers were obtained using a 325nm laser.

For the sub-set of samples with a fixed nucleation temperature of 300 °C but varying growth temperature from 260 – 360 °C, Figure 9 shows their PL spectra. The one with the smallest XRD peak (71 arcsec, ZT022511N grown at 300 °C) also shows the strongest PL intensity for the band edge emission, although its peak intensity is still substantially weaker (by a factor of 3.7) than a bulk ZnTe single crystal sample (serving as a reference). We also note that the peak energies of these epitaxial layers are slightly higher than that of the reference sample (by 7-8 meV), which is perhaps due to residual strain (lateral compressive).

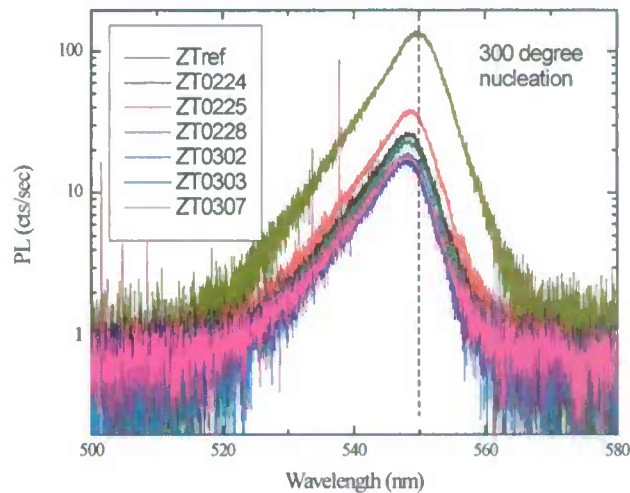


Fig.9 PL spectra of ZnTe epilayers grown at a fixed nucleation temperature 300 °C with varying growth temperature from 260 – 360 °C.

Figure 10 shows the PL spectra of another sub-set of samples grown at a fixed temperature 300 °C with varying nucleation temperature from 260 – 340 °C. The variation in PL intensity is relatively small, although the one with 340 °C nucleation temperature and a larger XRD width (83 arcsec, ZT031811N) seems to yield the highest PL intensity (not by much compared to the one with the smallest XRD peak). The PL intensities for all the samples shown in Fig.9 and Fig.10 are summarized in Fig.11, with varying XRD line width.

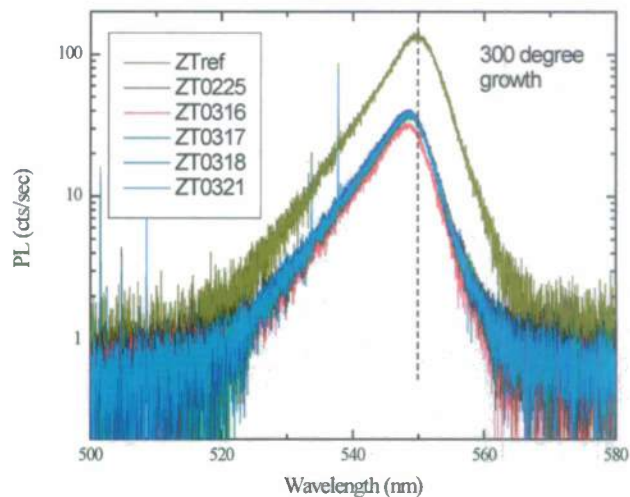


Fig.10 PL spectra of ZnTe epilayers grown at a fixed temperature 300 °C with varying nucleation temperature from 260 – 340 °C.

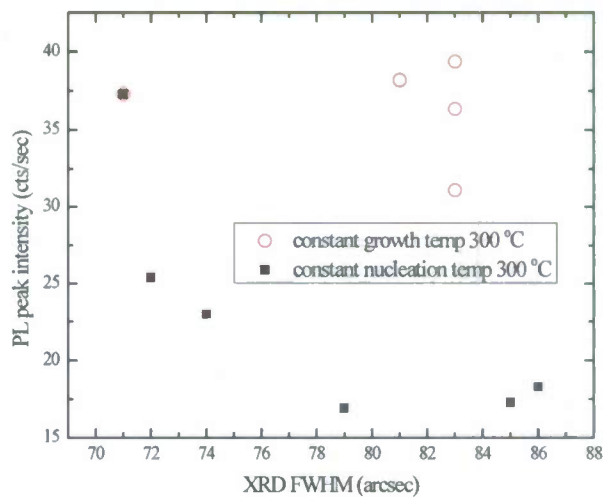


Fig.11 PL peak intensity vs. growth or nucleation temperature.

Extending to the spectral range below the band edge, in addition to the band-to-band emission (BB), these epilayers typically show a sub-bandgap (SBG) emission band with its peak energy at around 675 nm (1.837 eV). This band is likely related to defects or impurities. The PL spectra for the two sub-sets of samples are shown in Figure 12 and Figure 13. The intensity of the SBG band also depends strongly on the epitaxial nucleation and growth temperatures, but more or less tracking the BB emission for the nucleation dependence, as shown in Figure 14.

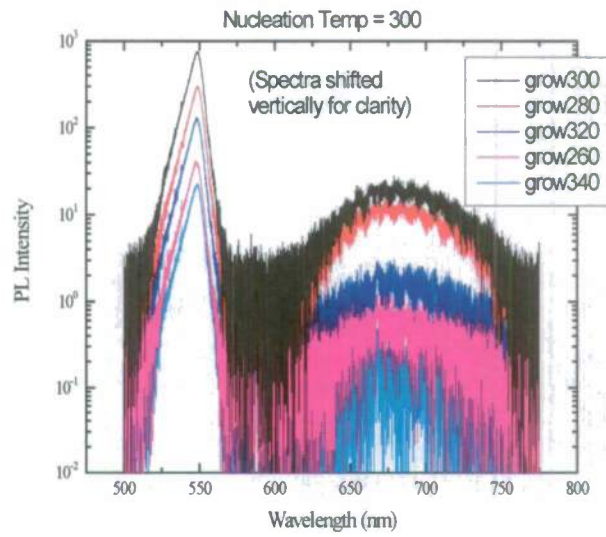


Fig.12 PL spectra of ZnTe layers with constant nucleation temperature but varying growth temperature.

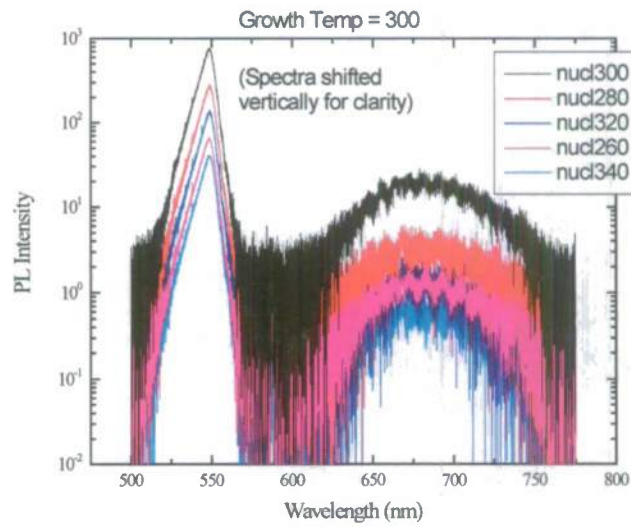


Fig.13 PL spectra of ZnTe layers with constant growth temperature but varying nucleation temperature.

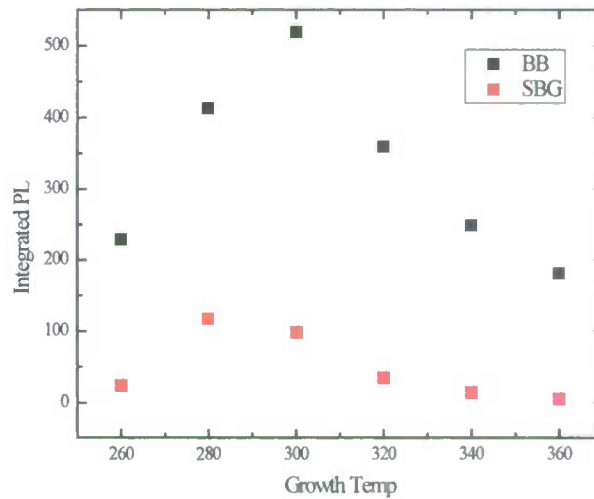


Fig.14 PL peak intensity vs. growth temperature for nucleation temperature of 300 °C.

B. Cleaved Edge-View Maps of BB and SBG Photoluminescence

The sample with nucleation temp = 300 and growth temp = 300 had the largest BB emission. The sample with nucleation temp = 300 and growth temp = 280 had the largest SBG emission. These two samples were cleaved to obtain photoluminescence maps along the growth axis.

022511 (nucleation temp = 300, growth temp = 300):

For these measurements, we used a 325nm laser with an approximate power density of 100 KW/cm². Both the BB emission and SBG emission intensity show depth dependence. The BB intensity peaks near the bottom of the epilayer (close to the substrate), whereas the SBG peaks close to the top surface, as shown in Figure 15 for the relative intensities at three depths, and Figure 16 for the BB emission intensity and the SBG/BB ratio vs. depth. These results seem to suggest more defects or impurities were introduced at longer growth time.

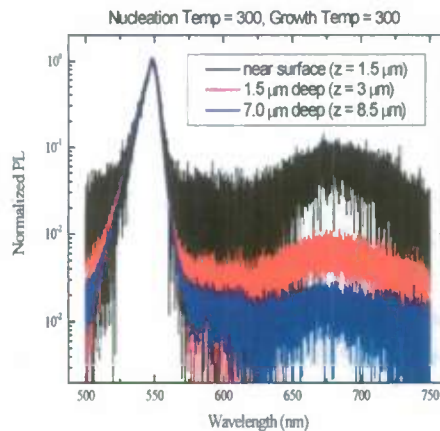


Fig. 15 Normalized PL spectra at different depths.

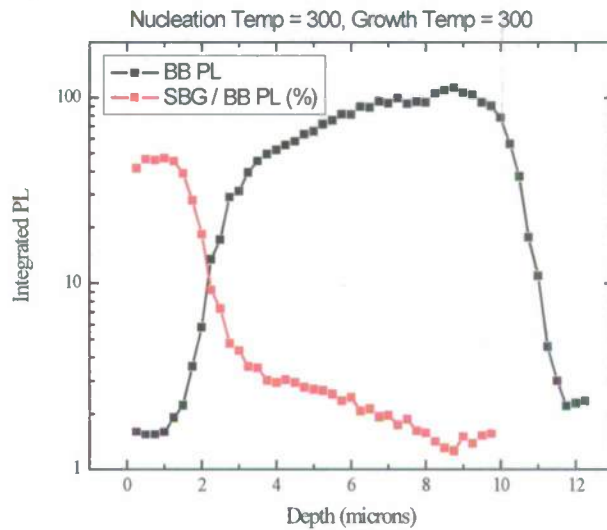


Fig.16 Variation of the band edge emission with depth, and the variation of the SBG/BB ratio with depth.

022411 (nucleation temp = 300, growth temp = 280):

For these measurements, we used a 532nm laser in three power levels (after the 325nm died). Figure 17 shows PL spectra with varying excitation power, showing that the SBG emission is saturating with increasing power. Figure 18 shows the variation of the spectra at different depths from the top surface. The exact physical location of the surface was not precisely determined (which needs to be calibrated in the future), but the relative positions are accurate. Again, the SBG emission is stronger when approaching the top surface, similar to the other sample. Figure 19 shows that the SBG/BB ratio also depends on the depth: the density of the defects or impurities is lower in the deeper part, thus easier to be saturated.

The results of the both samples indicate that the more defects or impurities were incorporated into the film in the later stage of the growth.

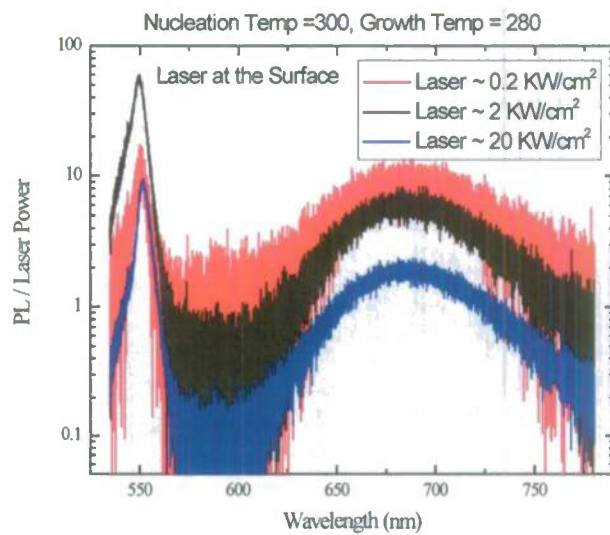


Fig.17 PL spectra at different excitation power at a depth close to the surface.

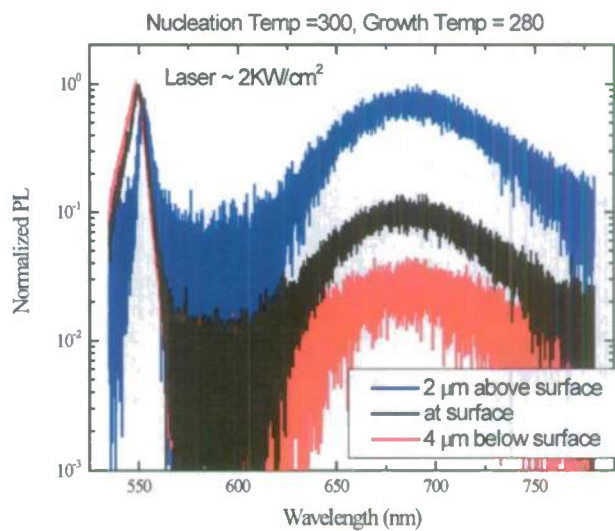


Fig.18 PL spectra at different depths from the top surface.

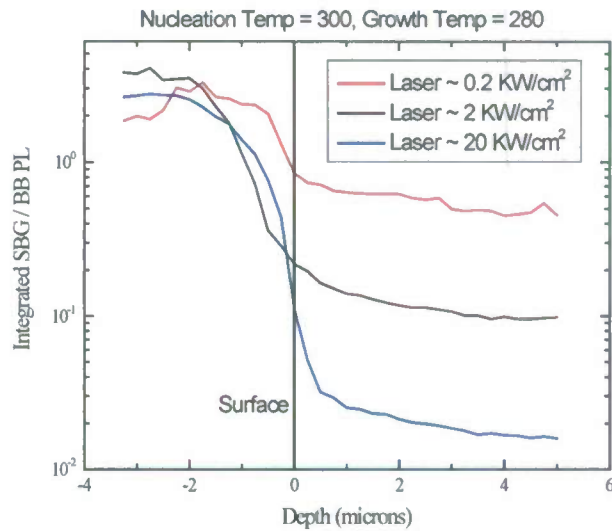


Fig.19 SBG/BB ratio vs. depth for different excitation densities.

C. Two-Dimensional Plan-View Maps of BB Photoluminescence Intensity

We did low spatial resolution PL mapping measurements for all the samples as a quick survey. Figure 20 shows one example for ZT022511N. In the future, higher resolution measurements should be performed in conjunction with modeling as mentioned for the CdTe section, hoping to extract the carrier diffusion length in the material.

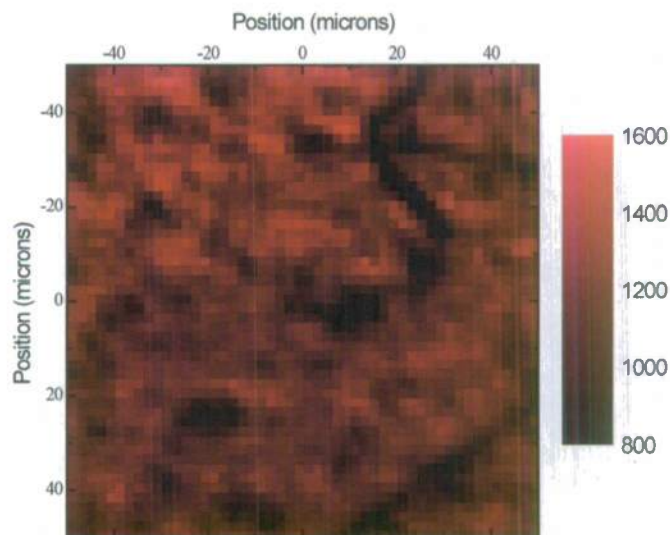


Fig.20 PL mapping of a ZnTe epilayer (ZT022511N).

7. MCT epilayer transmission and reflection measurements

A. Transmission and Reflectance

We have recently set-up a multi-purpose broad band IR system that covers a spectral range from 2 to 20 μm . It can perform Transmission, Reflectance, photo-modulation spectroscopy (this function has not been tested yet), photoluminescence (no cryostat at this time, thus not very useful for the IR materials of interest). A set of MCT epilayers were provided by Dr. Gregory Brill (ARL). The transmission spectra, Figure 21, clearly show the bandgap variation, qualitatively increasing in the order of R31716A, R31716T2, R31716T1, and R2003. The explicit bandgap values could be obtained by fitting to the widely used formula $\alpha^2 \propto E - E_g$. However, this model is incorrect, because it neglects the excitonic effect. Even it is usable, one still encounters the ambiguity as to include which portion of the data in the fitting. Modulation spectroscopy, either in the reflectance or transmission mode, can to some extent remove the ambiguity, i.e., giving a better defined bandgap. We plan to test the modulation spectroscopy later. The linear reflectance spectra, Figure 22, are not very useful for the purpose of determining the bandgap, because of the complication of the interference effect.

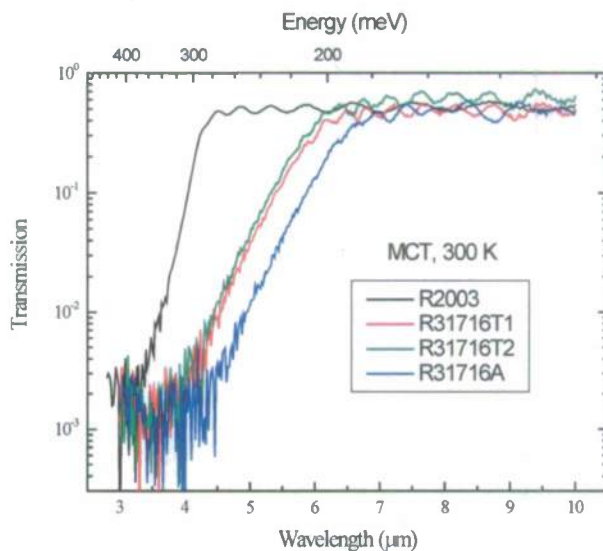


Fig.21 Transmission spectra of MCT samples measured at 300 K.

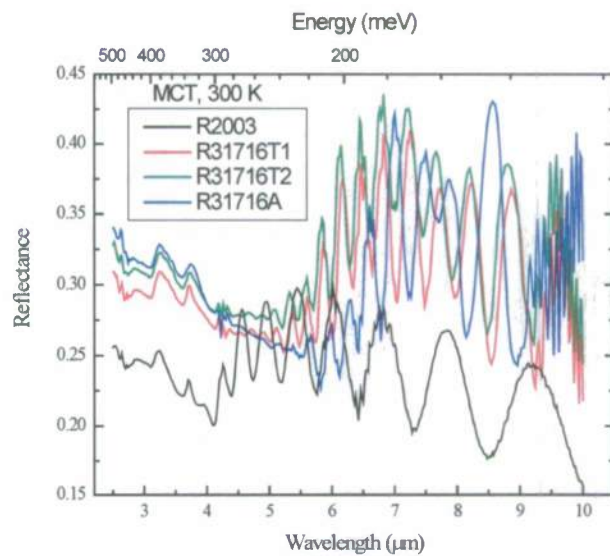


Fig.22 Reflectance spectra of MCT samples measured at 300 K.

B. Photoluminescence

We made several attempts to measure the photoluminescence spectra of these samples at 77K with an FTIR spectrometer at Davidson College, but we were unable to detect any signal. Compared to other samples, such as InGaAs alloy, measured from the same system, the PL signal from these MCT samples are likely very weak.

C. Raman Spectroscopy

We made several attempts to measure the Raman spectra of these samples, but the signals were very weak such that it was difficult to distinguish from the artifacts of the spectroscopy system. In fact, MCT is known to have very small Raman cross section as reported in the literature. We are making effort to correct the artifacts of the spectroscopy system, and will measure them again in the future.